Melting properties of the refractory metals V and W and the binary VW alloy fully from first principles

Li-Fang Zhu [ORCID],[1,2,*] Prashanth Srinivasan,[2] Yilun Gong [ORCID],[1] Tilmann Hickel [ORCID],[1,3]
Blazej Grabowski [ORCID],[2] Fritz Körmann [ORCID],[1,3] and Jörg Neugebauer [ORCID][1]

[1]*Department for Computational Materials Design, Max-Planck-Institut für Eisenforschung GmbH, 40237 Düsseldorf, Germany*
[2]*Institute for Materials Science, University of Stuttgart, 70569 Stuttgart, Germany*
[3]*BAM Federal Institute for Materials Research and Testing, 12489 Berlin, Germany*

We investigate the melting properties of the bcc refractory metals V and W, and the disordered equiatomic VW alloy from first principles. We show that thermal vibrations have a large impact on the electronic density of states (DOS) and thus considerably affect the electronic contribution to the free energy. For W, the impact of vibrations on the electronic free energy of solid and liquid is different. This difference substantially impacts the computed melting point and also triggers a large electronic heat capacity difference between solid and liquid. For V, although vibrations likewise affect the electronic free energy, the effect on the melting properties cancels out to a large degree. For the binary VW alloy we observe a similar impact as for W, but slightly weaker. The underlying physics is explained in terms of the electronic DOS of the solid and liquid phases. Based on our accurate first-principles results, we reveal critical limitations of the Sommerfeld approximation in predicting the electronic heat capacity difference between solid and liquid. Our results thus prompt us to scrutinize this approximation which is often used in phase diagram parametrizations in the CALPHAD approach, as well as for materials, such as W, that have a large electronic DOS difference between solid and liquid at the melting temperature.

I. INTRODUCTION

Melting properties of materials, such as the melting temperature, entropy, and enthalpy of fusion, are key parameters for materials design. They are essential to determine the lattice stability, a quantity that provides the basis for all multicomponent phase diagrams, in particular within the CALPHAD method [1–3]. The melting point of a material is also a key quantity in searching for high-performance refractory materials. Recently, bcc refractory high-entropy alloys, e.g., VNbMoTaW, were shown to have superior high-temperature mechanical properties [4–6]. They are expected—but not yet confirmed—to have high melting temperatures based on the finding that a high melting point correlates with high-temperature strength in such alloys [7].

Experimental measurements of melting properties of bcc refractory alloys and their unary components are challenging, exactly due to the high melting temperatures. For example, the reported experimental enthalpies of fusion are significantly scattered, even for the unary metals V and W. The values range from 17 to 28 kJ/mol for V [8–10] and from 35 to 61 kJ/mol for W [11–15]. Since some of the unary data are selected as input to the CALPHAD method, their uncertainty eventually results in large uncertainties in the extrapolated phase diagrams and thermodynamic properties of *all* dependent multicomponent systems.

An alternative to experimental measurements is the calculation of the melting properties from *ab initio* based on density functional theory (DFT). The main challenge in *ab initio* simulations is the accurate calculation of the free energy of both solid and liquid by taking into account all relevant entropic contributions, i.e., atomic vibrations including the anharmonic contribution and electronic excitations including the electron-vibration coupling. The anharmonic contribution and the electron-vibration coupling in bcc metals have generally a more complex temperature dependence compared to fcc metals [16]. Importantly, their impact on the free energy of solid and liquid may be different, thus affecting the solid-liquid transition temperature. For example, based on *ab initio* derived potentials, Moriarty [17] found that the electron-vibration contribution to the solid and liquid free energies lowers the calculated melting temperature of bcc Mo from ∼7000 K to 3528 K (experiment: 2883 K).

For many metals, the electronic contribution to the heat capacity difference between solid and liquid at the melting point is small [18,19]. One exception is W, where this difference was reported to be 0.5 k_B/atom [18–20] based on

*Corresponding author: l.zhu@mpie.de;
lifang.zhu@imw.uni-stuttgart.de

the Sommerfeld (SOM) approximation [21,22] using the electronic density of states (DOS) of the solid and liquid evaluated in Refs. [17,23,24]. The Sommerfeld model has been widely used to calculate the electronic free energy and the electronic heat capacity due to its high efficiency by considering only the temperature independent DOS at the Fermi level. However, the predictions from the Sommerfeld approximation are usually not in quantitatively good agreement with experiment, even if an accurate electronic DOS determined from electronic structure calculations is used. Instead, *ab initio* molecular dynamic (MD) simulations can accurately predict the electronic free energy and the electronic heat capacity by taking into account all relevant physical contributions. Zhang *et al.* [25] applied this approach to bcc W and found that the electronic contribution to the free energy strongly increases in magnitude with temperature due to thermal vibrations. However, due to the severe computational cost of these methods, *ab initio* studies on the liquid free energy of bcc refractory metals, on the electronic contribution difference between solid and liquid free energy and on the influence of the contribution on their melting properties are scarce.

A suitable alternative for accurately calculating melting properties is the *ab initio* free-energy approach [26–30]. It is based on *ab initio* computed Gibbs energies of the solid and liquid from which the melting point and melting properties can be determined. Though in principle providing DFT accuracy, this approach faces two major challenges: the high computational cost and the reliance on a good reference system for the involved thermodynamic integration (TI). These challenges can be overcome by utilizing the *two-optimized reference thermodynamic integration using Langevin dynamics* (TOR-TILD) methodology [31,32]. The computational efficiency of TOR-TILD has been demonstrated for unary fcc metals Al, Cu, and Ni, preserving an *ab initio* accuracy of 1 meV/atom [31,32]. However, applications of TOR-TILD have so far been limited to unaries and its applicability to alloys has not yet been evaluated.

Here we apply TOR-TILD to calculate the melting properties for the bcc refractory metals V and W and for the disordered equiatomic binary VW alloy based on a bcc lattice. V and W are important refractory materials and their melting temperatures have been computed previously with *ab initio* MD. For example, Wang *et al.* [33] calculated the melting point of W using the free-energy correction approach and a direct *ab initio* MD simulation on the solid-liquid coexisting system. For V, the melting curves at high pressures were computed with the two-phase modeling [34] and with a combined approach of the two-phase method and the modified-Z method [35]. However, these studies focused only on the melting point and, moreover, did not evaluate the impact of electronic excitations and their coupling to vibrations on the melting properties. Also, there is not yet a detailed study on the melting properties of the binary VW alloy from *ab initio* MD. In the present work, besides computing various melting properties for V, W, and VW, the impact of vibrations on the electronic free energy, the electronic contribution difference to solid and liquid and the influence of this difference on the melting properties are also investigated. Based on our *ab initio* MD results, the limitations of the Sommerfeld approximation in predicting the electronic free energy and the electronic

heat capacity are discussed. Further, the performance of two exchange correlation functionals, the local-density approximation (LDA) and the generalized gradient approximation (GGA), in predicting melting properties of the three investigated systems are compared and discussed.

II. METHODOLOGY

Within the TOR-TILD methodology, the Gibbs energies of the solid and liquid need to be calculated. In the following, we describe the most relevant aspects of the solid (Sec. II A) and liquid (Sec. II B) free-energy calculations. Considerations on the configurational entropy for the VW binary are given in Sec. II C. The utilized computational software and parameters are given in Sec. II D.

A. Solid free energy

To accurately capture the solid free energy, all relevant excitation mechanisms should be carefully considered; quasiharmonic and anharmonic atomic vibrations, electronic excitations for the static lattice, and the electron-vibration coupling. The quasiharmonic contribution and the electronic contribution for a static lattice can be calculated straightforwardly [36]. Computationally most challenging are the anharmonic free-energy calculations including the electron-vibration coupling, generally carried out by TI calculations [37–39].

In the present work we mainly rely on the *two-stage upsampled thermodynamic integration using Langevin dynamics* (TU-TILD) method [39] to calculate the solid anharmonic free energy. This method utilizes a specially designed interatomic potential (labeled "ref") as an intermediate reference to separate the TI into two stages, first from the quasiharmonic system to "ref" and second from "ref" to the *ab initio* solid. The free-energy surface of "ref" is calculated on a dense set of volumes and temperatures and used later for the liquid free-energy calculation (where "ref" is labeled "ref1"). As "ref" is fitted to accurately represent the high-temperature *ab initio* solid, it can significantly reduce the number of *ab initio* MD steps to reach the convergence. To further speed up the TI calculations from "ref" to the *ab initio* solid, the upsampling technique [37] is applied, i.e., first performing *ab initio* MD simulations with low DFT parameters (*k* points and cutoff) and second running static calculations with high DFT parameters on a few uncorrelated snapshots from the MD trajectories to correct the error introduced in the first step. The details of the TU-TILD method are discussed in Ref. [39].

The TU-TILD method uses the embedded atom method (EAM) or the modified embedded atom method (MEAM) potentials as the intermediate reference for TI. This approach has shown remarkable efficiency for calculations on unary fcc metals, such as Cu, Al, and Ni [31,32]. When going to bcc-based refractory materials with complex temperature-dependent anharmonic contributions, machine learning potentials show better performance than EAM/MEAM potentials with respect to computational efficiency [40,41]. Since machine learning potentials, specifically moment tensor potentials (MTPs) [42], can accurately predict the DFT energies and forces even for multicomponent materials, they allow

one to substitute the expensive TI to DFT by more efficient free-energy perturbation calculations for computing the solid anharmonic free energy without sacrificing *ab initio* accuracy [40,41,43]. A method proposed recently along these lines was termed the "direct upsampling" approach [41]. Its efficiency enables to access a dense free-energy surface to derive accurate thermodynamic properties. We have tested this approach for calculating the solid free energy of binary VW using GGA. The Gibbs energies and thermodynamic properties from direct upsampling agree well with those from the TU-TILD method but can be obtained at significantly reduced computational cost. Detailed discussions on the accuracy, efficiency, and implementation of direct upsampling are documented in Ref. [41].

The vacancy contribution can be important for investigating thermodynamic material properties. It is accessible using the developments in Refs. [37,38]. For bcc V and W, the contribution of vacancies to the total free energy was shown to be negligible for bulk thermodynamic properties even at the melting point [44]. Therefore, it is not considered in the present work.

B. Liquid free energy

Free-energy calculations for the liquid are more challenging than for the solid because of the absence of a static reference lattice. TI from an appropriate reference system therefore plays a crucial role for such calculations [26–32]. In particular, the free energy of the reference system needs to be easily accessible. Further, the proximity of the reference system to the *ab initio* liquid directly affects the computational efficiency. In the present work, we calculate the liquid free energies utilizing TOR-TILD [31], where two optimized references ("ref1" and "ref2") are used to speed up the calculations (hence "TOR"). Both references are EAM potentials fitted using the MEAMfit code [45]. The first reference "ref1" is fitted to *ab initio* solid energies and used for the solid free-energy calculations in the aforementioned TU-TILD method. The solid free-energy surface of "ref1" is used as a starting point to obtain the liquid free-energy surface of "ref2" by the interface method [46] and TI between "ref1" and "ref2". Since "ref2" is specially fitted to the *ab initio* liquid energies, the TI from "ref2" to the *ab initio* liquid is very efficient. Additionally, the upsampling technique is applied for further improving the computational efficiency. Note that electronic excitations and their adiabatic coupling to atomic motion for the liquid phase are fully implicitly included during the TI calculations from "ref2" to the *ab initio* liquid. Further details about the TOR-TILD methodology can be found in Ref. [31].

C. Configurational entropy

For alloys, such as the here considered VW binary, the configurational entropy needs to be accounted for in both solid and liquid free-energy calculations. In general, this contribution will affect the melting properties, which derive from free-energy differences. However, as discussed below, for the specific alloy system considered here, this contribution largely cancels out.

V and W are known to be soluble in the solid phase over the full composition range [47]. It is therefore reasonable to assume an ideally disordered solid solution for the melting property calculations. To validate this assumption, we apply the low-rank potential (LRP) method [48–50] together with Monte Carlo (MC) simulations to compute the temperature-dependent ordering tendency of solid VW. The LRP training is performed as proposed in Ref. [48]. For the initial training, 10 special quasirandom structures (SQS) [51] with a supercell size of $3 \times 3 \times 3$ (in terms of the cubic unit cell) are generated and the corresponding energies are calculated with DFT (using the GGA functional). As the main scope is the high-temperature regime, an electronic smearing temperature of 3000 K and a lattice constant of 3.22 Å are employed, the latter being in between our computed values for the solid and liquid at this temperature. As in Ref. [48], an ensemble of 10 LRPs is trained. Using this ensemble of LRPs, 10 independent MC simulations are carried out for the same $3 \times 3 \times 3$ supercell size. New configurations for retraining the potentials are generated from temperature regimes, where the calculated specific heat capacity, a direct outcome of the MC simulations and a sensitive measure for the phase stability and short-range order, differs significantly among the 10 potentials. The resulting 50 new atomic configurations are then added to the training and validation set to retrain the LRP ensemble. Based on the retrained potentials, the resulting MC simulations do not show any significant deviations among the 10 potentials. The final training and validation sets are respectively 54 and 6 with a training error of ∼0.2 meV/atom and a validation error of ∼0.5 meV/atom.

Using the 10 LRPs trained according to the above procedure, we performed 10 independent MC simulations on larger $8 \times 8 \times 8$ supercells with 1024 atoms. The temperature was varied between 10 to 3000 K with steps of 10 K. The resulting configurational part of the specific heat capacity C_V for solid VW is shown in Fig. 1(a) and we observe a phase transition at 330 K. The low-temperature ground state for the binary VW is the B32 structure as shown in Fig. 1(a). It is consistent with the finding in Refs. [52,53].

In order to be able to quantify the ordering tendency for both solid and liquid, we introduce the concept of the fraction of atomic pairs (FAPs). The FAPs are defined as N_{ij}/N_{total}, where N_{ij} is the number of pairs between atom i and j and N_{total} the total number of all pairs within a given cutoff r. For the binary VW alloy, there are V-V, W-W, V-W, and W-V pairs (the latter two being symmetrically equivalent) in the structure. When each of these pairs has a similar probability to show up in the structure, i.e., FAP $\approx 1/4$, the structure can be assumed to be disordered. The FAPs thus convey the same information as the conventional Warren-Cowley short-range order (SRO) parameters [54,55]. However, the FAPs can be consistently utilized when characterizing the liquid structure, while this is not possible for the normal definition of the SRO parameters. To compute the FAPs for solid VW in Fig. 1(b), we utilize a cutoff of $r = 4$ Å for which the first two nearest neighbors of the solid [corresponding to the first peak in the pair distribution function $g(r)$ of the liquid] are enclosed. The FAPs confirm the occurrence of an order-disorder transition at low temperatures. As the temperature interval considered for the VW binary alloy (2600 to 3000 K) is way above
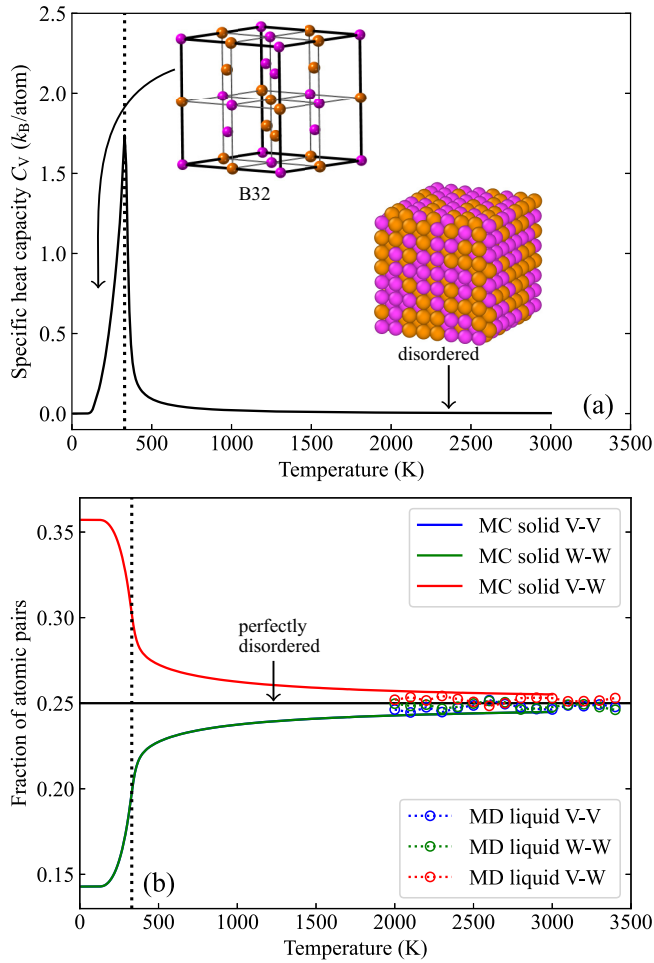
FIG. 1. (a) Temperature dependence of the configurational part of the specific heat capacity C_V computed from MC simulations using the LRP for the solid binary VW alloy. The sharp peak indicates an order-disorder phase transition. The ground-state B32 structure and the high-temperature disordered structure are indicated. (b) The FAPs for solid VW (solid lines) calculated from the MC simulations and for liquid VW (dotted lines with circles) from MD simulations.

the transition temperature of 330 K, the solid can be safely assumed to be fully disordered.

V and W are also known to be well soluble in the liquid phase [47]. This is to be expected based on the good solubility already in the solid phase. It is thus reasonable to also assume a randomly disordered liquid solution for the melting property calculations. A proper calculation of the configurational entropy for the liquid is challenging, due to the randomly distributed atomic positions on top of the chemical disorder. The LRP method is limited to a reference lattice and thus not suitable for the liquid. As an estimate, we perform *NPT* MD simulations for the liquid with an MTP [42] fitted to our *ab initio* liquid data. The training dataset for the MTP includes 1600 uncorrelated configurations from our *ab initio* MD trajectories computed with GGA. The corresponding volumes and temperatures for these configurations are consistent with those used for computing the DFT liquid free-energy surface in Table I.

Applying the fitted MTP we perform MD simulations on liquid VW using a supercell of $8 \times 8 \times 8$ with 1024 atoms. The simulation time is 100 ps. Ten uncorrelated snapshots from an equilibrated part of the MD simulations are utilized to compute the averaged FAPs at each temperature with a cutoff of 4 Å. As shown in Fig. 1(b), the FAPs for the liquid fluctuate around 0.25 and exhibit no correlations within the investigated temperature range. Thus, similarly as for the solid, the VW liquid can be considered to be fully disordered for the melting property calculations.

Based on the above arguments, we assume perfect chemical disorder for both solid and liquid VW for the melting analysis. The configurational energy is captured by utilizing a random distribution of the V and W atoms. For the small supercells required for the DFT simulations, the random distribution is modeled by SQS structures. For a 128 atom supercell the energy differences between different SQS are in the range of only 3 meV/atom. For the configurational entropy, we utilize the ideal mixing term for both solid and liquid (specifically, $-k_B T \ln 0.5$ for the 50:50 composition). It therefore cancels in the differences relevant for the melting properties.

D. Computational details

For all our DFT calculations we use the projector-augmented wave (PAW) method [56] as implemented in VASP [57–60]. PAW potentials with 11 and 14 valence electrons are used for V and W, respectively. LDA and GGA are employed for the exchange-correlation functional, with the Perdew-Burke-Ernzerhof (PBE) [61] parametrization for GGA. The sets of explicitly DFT computed volume and temperature points for the solid and liquid free-energy surfaces are given in Table I. For all three systems, the DFT solid and liquid calculations are performed in a $4 \times 4 \times 4$ supercell with 128 atoms. For the binary VW alloy, an SQS is employed for the solid. This SQS structure is then heated up to 3500 K, in order to obtain the liquid structure. The explicitly computed DFT volume-temperature points are used as input to fit polynomials up to third order to obtain an analytical description of the free-energy surface as a function of volume and temperature. As mentioned in Sec. II A, the upsampling technique [37], i.e., applying high DFT parameter calculations on a few (typically 10) snapshots taken from the *ab initio* MD simulations with low DFT parameters, is used to speed up the TI calculations. For V, the plane wave cutoff and k point mesh (Monkhorst-Pack [62]) are set to 300 eV and $2 \times 2 \times 2$, respectively, for the low converged calculations, and 400 eV and $5 \times 5 \times 5$, respectively, for the high converged calculations. For W and VW, the plane wave cutoff and k point mesh (Monkhorst-Pack [62]) are set to 320 eV and $2 \times 2 \times 2$, respectively, for the low converged calculations, and 400 eV and $5 \times 5 \times 5$, respectively, for the high converged calculations.

For the reference potential calculations we use the LAMMPS software package [63]. As mentioned in Sec. II B, the interface method [46] is employed to calculate the melting points of the "ref1" potentials, T_{ref1}^m. For V and W, a tetragonal $13 \times 13 \times 26$ supercell with 8788 atoms is used resulting in $T_{\text{ref1}}^m = 2046$ K for V (experiment: 2183 K) and $T_{\text{ref1}}^m = 3319$ K for W (experiment: 3687 K). For the binary

TABLE I. Meshes of explicitly computed volumes V (per atom), and temperatures T, used for the thermodynamic integration from the optimized potentials to DFT for V, W, and VW. The volumes are additionally expressed in terms of a corresponding bcc lattice constant $a = (2V)^{1/3}$.

			Solid	Liquid
V	LDA	V (Å³)	12.58, 12.84, 13.10, 13.37, 13.64	13.37, 13.64, 13.91, 14.19, 14.47
		a (Å)	2.93, 2.95, 2.97, 2.99, 3.01	2.99, 3.01, 3.03, 3.05, 3.07
		T (K)	2000, 2200, 2400, 2600	2000, 2200, 2400, 2600
	GGA	V (Å³)	13.64, 14.05, 14.47, 14.90	14.90, 15.04, 15.33, 15.63, 15.78
		a (Å)	3.01, 3.04, 3.07, 3.1	3.1, 3.11, 3.13, 3.15, 3.16
		T (K)	1800, 2000, 2200, 2400	1800, 2000, 2200, 2400, 2600
W	LDA	V (Å³)	14.47, 14.90, 15.33, 15.78, 16.23	15.78, 16.23, 16.69, 17.16, 17.64, 18.13
		a (Å)	3.07, 3.1, 3.13, 3.16, 3.19	3.16, 3.19, 3.22, 3.25, 3.28, 3.31
		T (K)	3400, 3600, 3800, 4000, 4200	3400, 3600, 3800, 4000, 4200
	GGA	V (Å³)	16.23, 16.54, 16.85, 17.16	17.16, 17.48, 17.81, 18.13, 18.46
		a (Å)	3.19, 3.21, 3.23, 3.25	3.25, 3.27, 3.29, 3.31, 3.33
		T (K)	3000, 3200, 3400, 3600	3000, 3200, 3400, 3600
VW	LDA	V (Å³)	14.33, 14.61, 14.90, 15.19	14.90, 15.19, 15.48, 15.78
		a (Å)	3.06, 3.08, 3.1, 3.12	3.1, 3.12, 3.14, 3.16
		T (K)	2800, 3000, 3200, 3400	2800, 3000, 3200, 3400
	GGA	V (Å³)	14.90, 15.19, 15.48, 15.78	15.78, 16.08, 16.38, 16.69
		a (Å)	3.1, 3.12, 3.14, 3.16	3.16, 3.18, 3.20, 3.22
		T (K)	2400, 2600, 2800, 3000	2400, 2600, 2800, 3000

VW alloy, a tetragonal $16 \times 16 \times 32$ supercell based on the 128-atom SQS structure with 16 384 atoms is employed. The calculations result in a melting temperature $T_{\mathrm{ref1}}^{m} = 2421$ K. The corresponding CALPHAD value is 2780 K, which is obtained by taking the crossing point of the solid and liquid Gibbs energies extrapolated using Thermo-Calc 2023a [64], as detailed in Sec. III C. The "ref1"potentials for all three systems are fitted to *ab initio* MD trajectories of the corresponding solid using the GGA-PBE exchange-correlation functional. Our previous studies [31,32] and the results below show that the GGA-PBE functional predicts lower melting points compared to experimental data due to its underbinding property. Here this tendency is also reflected in the melting points predicted by the empirical potentials since they have been fitted to PBE calculations. The other reference potential calculations are performed in a cubic $15 \times 15 \times 15$ supercell with 6750 atoms for V and W, and a cubic $16 \times 16 \times 16$ supercell with 8192 atoms for the VW binary alloy. For fitting the liquid free-energy surface of "ref2," we use the same volumes as for the DFT calculations (see Table I) but at a denser temperature mesh (steps of 5 K).

For the *ab initio* and classical MD simulations we use a time step of 5 fs and the Langevin thermostat with a friction parameter of 0.01 fs^{-1} to control the temperature.

III. RESULTS AND DISCUSSION

Figures 2–4 present our main results, the calculated melting properties for V, W, and VW. The Gibbs energies are referenced with respect to the energy of bcc V, W, and binary SQS VW at $T = 0$ K. The melting temperatures can be determined by the crossing point of the solid and liquid Gibbs energies. Note that for alloys, in contrast to unaries, the solidus and liquidus temperature usually do not coincide

resulting in a melting interval with an upper (liquidus) and lower (solidus) limit (see the cross symbols in Fig. 5) where the alloy consists of solid and liquid phases simultaneously. Within the CALPHAD community the crossing point of the solid and liquid Gibbs energy is defined as T_0 (without taking into account the partitioning of elements). However, to avoid confusion and be consistent with bcc V and W, in the present work the term "melting temperature" is nevertheless used for the binary VW.

A. Vanadium

In our previous work we found that, for fcc Cu, Al, and Ni, the melting points predicted by the GGA-PBE and LDA functionals provide a lower and upper bound for their experimental melting temperatures [31,32]. The underlying reason is the overbinding/underbinding property of LDA/PBE. The LDA functional generally yields smaller lattice constants and stiffer bulk moduli and phonon frequencies compared to experiment and PBE [36]. Therefore, the stiffer LDA system is more resistant to melting and exhibits a higher melting temperature. Here we find a similar behavior for bcc V that LDA results in a higher melting point (2230 K) and PBE provides a lower one (2140 K), as shown in Figs. 2(a), 2(b), and 5. Our predictions form a bound around the experimental melting point of 2183 K with a relatively small shift (-2% for PBE and $+2\%$ for LDA).

Prior works on fcc Al, Cu, and Ni [36,65] indicate that the $T = 0$ K lattice constants and bulk moduli predicted from PBE and LDA provide a reliable *ab initio* confidence interval for the corresponding experimental data. However, our current calculations for bcc V using both functionals predict smaller lattice constants and larger bulk moduli than the experimental values (see Table II). The same result was also obtained by
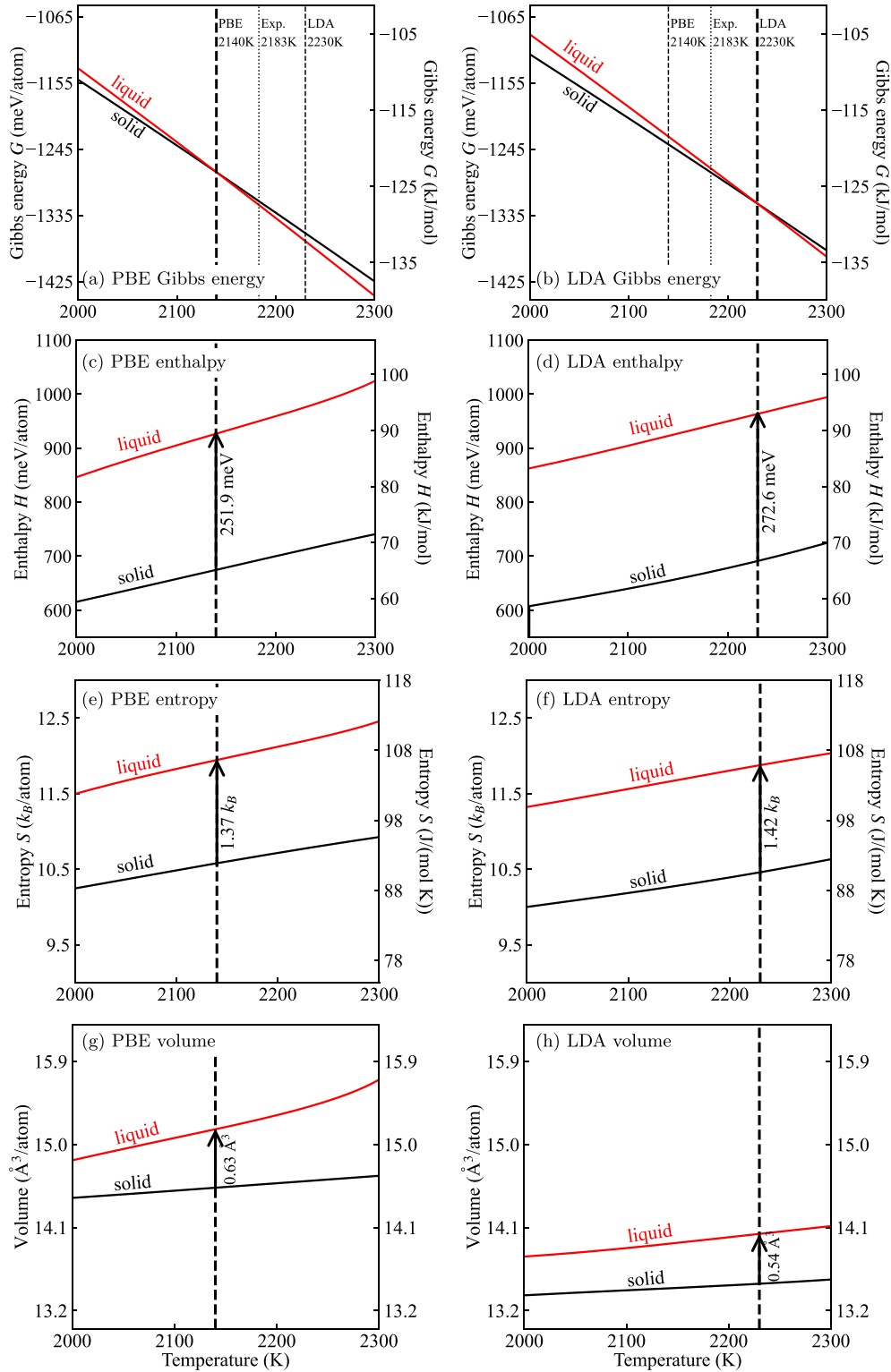
FIG. 2. Temperature dependence of various thermodynamic properties of solid and liquid V using PBE and LDA.

Haas *et al.* [65] for bcc V while using LDA and different GGA functionals including PBE. In our study this property is inherited even at high temperatures in the volume expansion of bcc V. As shown in Fig. 6, the volumes of bcc V at the corresponding melting temperature from both LDA and PBE

calculations locate below the experimental data [66]. Recent studies on bcc V [67,68] indicate that this could be a result of strong electronic correlations, not fully captured by standard DFT. Indeed, the 0 K equilibrium lattice constant predicted by PBE employing the dynamical mean field approach is 3.061 Å
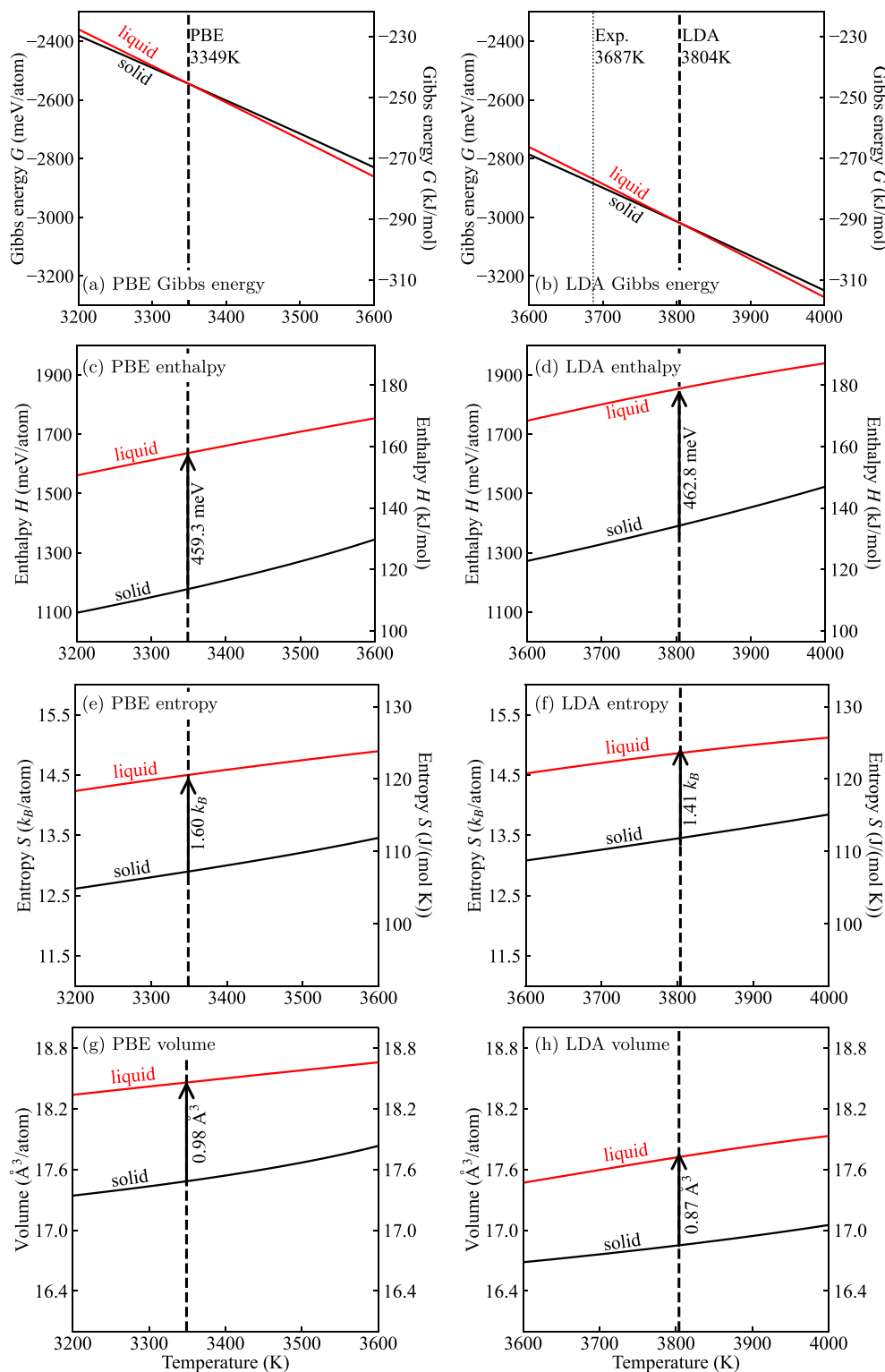
FIG. 3. Temperature dependence of various thermodynamic properties of solid and liquid W using PBE and LDA.

[68]. This value overestimates the lattice constant compared to the experimental value (3.027 Å [69]) as one usually would intuit for a PBE treatment. The good agreement between the experimental melting temperature and our predicted values using standard DFT for PBE and LDA indicates, however, that the impact of strong electron correlations likely cancels out in the melting temperature predictions. A similar observation has been made in our previous work on ferromagnetic Ni [32] for which magnetic contributions to solid and liquid free energies cancel out at high temperatures.
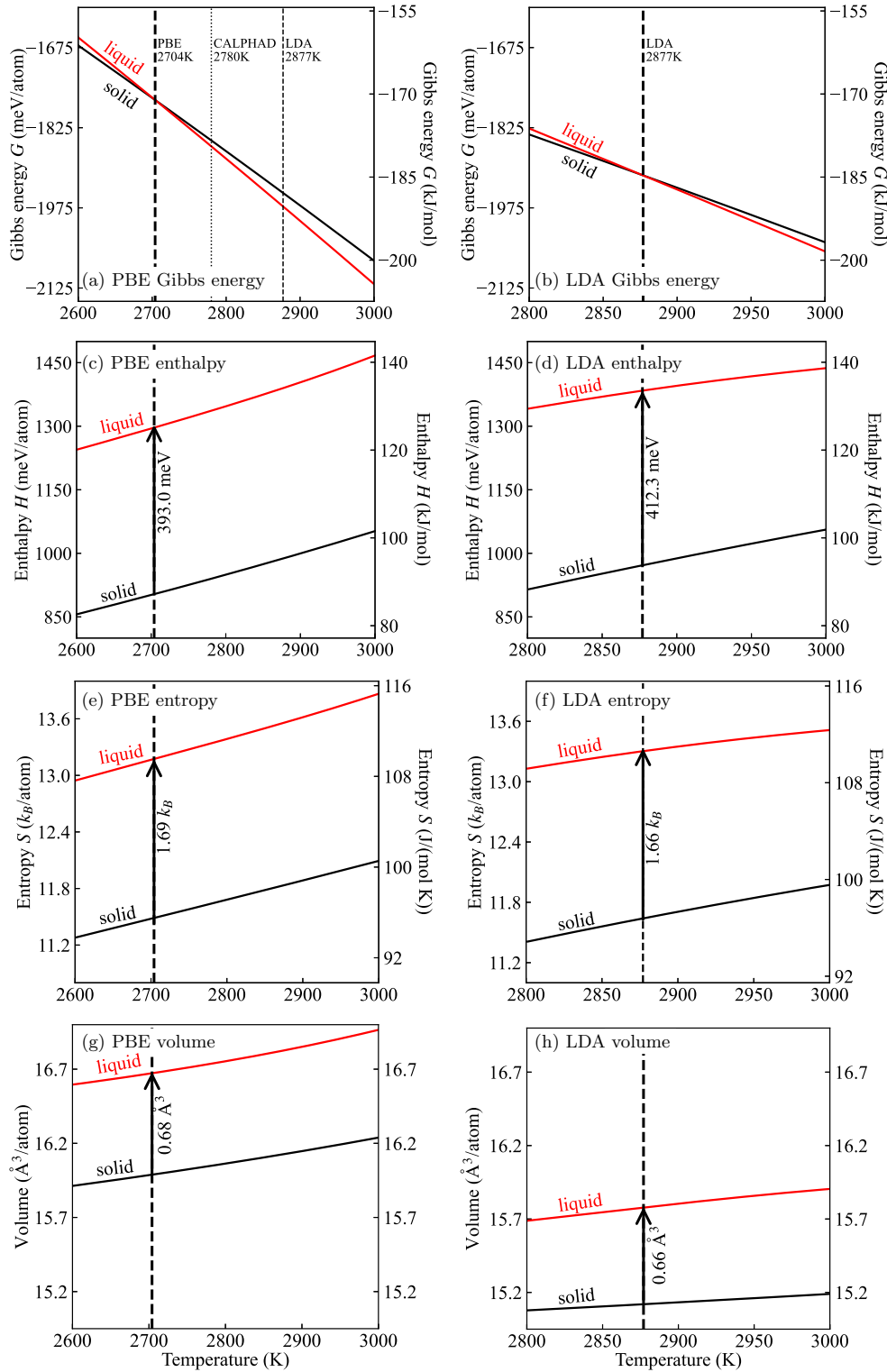
FIG. 4. Temperature dependence of various thermodynamic properties of solid and liquid VW using PBE and LDA.

Regarding other melting properties, e.g., the enthalpy and entropy of fusion, and the volume change at the melting point, the experimental data are rather scattered as shown in Table II. They do not fall in between our PBE and LDA predictions, but some of them are rather close to our DFT results. Overall, compared to using PBE as the exchange-correlation functional, the overbinding and thus stiffer LDA

system still predicts a higher melting point, larger enthalpy of fusion, smaller solid and liquid volumes, and smaller volume change at the melting point.

B. Tungsten

For bcc W, the experimental values of some of the properties fall in between our LDA and PBE predictions. This is,
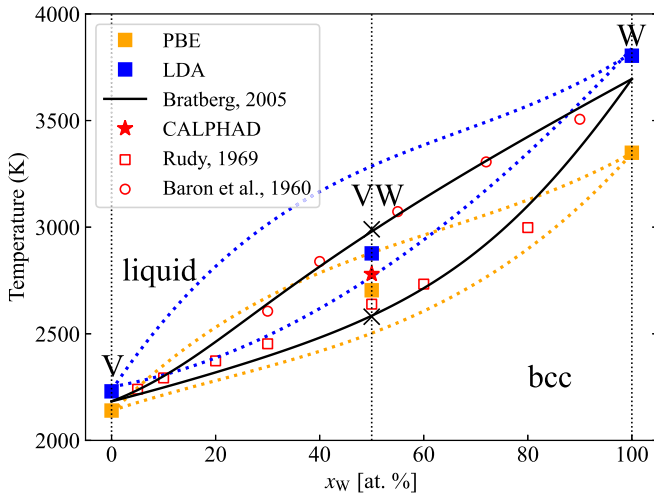
FIG. 5. Concentration-temperature binary phase diagram of V-W [47] constructed based on the measured incipient melting data for the solidus from Ref. [70] (red empty squares) and the measured data for the liquidus from Ref. [71] (red empty circles). The blue squares are the LDA data and the orange ones the PBE data. The red star is the melting temperature of the binary VW. It is given by the temperature at which the solid and liquid Gibbs energy extracted from the CALPHAD method cross. The dotted lines are the solidus and liquidus lines computed using our PBE (orange) and LDA (blue) Gibbs energies of V and W based on the ideal mixing approximation.

however, not true for all properties. For example, the melting points predicted from PBE (3349 K) and LDA (3804 K) encompass the experimental value (3687 K) as shown in Figs. 3(a), 3(b), and 5. The experimental 0 K lattice constant and bulk modulus also fall in between our PBE and LDA results (see Table II). This feature remains for the computed volumes at the melting temperature (see Fig. 6). However, the volume changes at the melting point from both PBE (0.97 Å^3/atom) and LDA (0.87 Å^3/atom) are smaller than the experimental data (1.35–1.81 Å^3/atom). The experimental enthalpy and entropy of fusion also fall outside the window of our PBE and LDA predictions. One needs to keep in mind that experimental measurements of melting properties are extremely difficult, and, consequently, the measured data are rather scattered. In contrast, our PBE and LDA results are consistent and provide more reliable predictions.

We find a strong impact of the electronic contribution on predicting the melting point of W. Neglecting the electronic contribution results in an upward shift of the melting temperature by 178 K for PBE (5% with respect to the experimental value) and 158 K for LDA (4% with respect to the experimental value), i.e., 3527 K for PBE and 3962 K for LDA. In an earlier work, Wang *et al*. computed the melting point of W also using GGA-PBE as the exchange-correlation functional [33]. They obtained 3450 K by the free-energy correction approach and 3465 K by directly simulating the solid-liquid coexistence. Both results are higher than our computed value of 3349 K and closer to our result without taking the electronic contribution into account. Additional sources for the discrepancy can be the difference in computational parameters. For example, in their calculations the p semicore states were treated as valence states, only the Γ point was

used for the Brillouin-zone sampling, and small cutoff energies (273 eV for the free-energy correction approach and 223 eV for the coexisting approach) were utilized. In our calculations we include both semicore s and p electrons as valence states because the W_{pv} potential suffers from ghost states at higher energies [25]. We also apply 400 eV as the cutoff energy and choose a $5 \times 5 \times 5$ k point mesh. Regarding the melting point shift induced by the electronic contribution, a similar phenomenon was reported for bcc Mo [17] where the predicted melting point with and without electron-vibration coupling was respectively 3528 K and $\sim$7000 K with a shift of 50%. The impact of the electronic contribution on the melting temperatures of the three investigated cases are discussed in detail in Sec. III D.

C. VW binary

Next, we test and analyze the performance of the TOR-TILD approach to describe the binary VW alloy with an equiatomic composition. Note that it is difficult to directly experimentally measure the melting temperature of VW (called as T_0 within the CALPHAD community). Therefore, in order to compare with our LDA and GGA predictions, we estimate an experimental value based on the available experimental data using the CALPHAD method. The phase diagram of V-W was obtained by Bratberg [47] based on the incipient melting solidus data of Rudy [70] and the liquidus measurements of Baron *et al*. [71], as shown in Fig. 5. Within Bratberg's work the temperature- and composition-dependent Gibbs energy curves for V-W alloys have been derived [47]. Based on the relevant thermodynamic parameters obtained by Bratberg including the SGTE database (Scientific Group Thermodata Europe) [72], we calculate the temperature-dependent Gibbs energies of the solid and liquid at the equiatomic composition using Thermo-Calc 2023a [64]. A melting point of 2780 K is then obtained from the crossing point of those two curves. Based on the Gibbs energies, we extract further melting properties such as enthalpy of fusion, entropy of fusion, and volume change at the melting point, as shown in Table II.

The melting temperature obtained by the CALPHAD method is once again located between our predicted PBE (2704 K) and LDA (2877 K) values as shown in Figs. 4(a) and 5. The relative shifts of our DFT predictions are rather small ($\sim$3%) compared to the CALPHAD value (2780 K). As mentioned in Sec. III A, for bcc V, both PBE and LDA predict smaller 0 K lattice constants and smaller volumes at high temperatures compared to the experimental data. Here, for the binary VW, due to the participation of V we observe a similar behavior of PBE and LDA as shown in Fig. 6. In particular, for both V and binary VW the PBE predictions closely reproduce the experimental data or our calculated CALPHAD values regarding the 0 K lattice constants and volumes at high temperatures. In Fig. 6 we provide the volumes at the corresponding melting temperatures of solid V, VW, and W from PBE and LDA calculations and from experiment or CALPHAD. They all follow Vegard's law, but the DFT predictions have a steeper slope than the experimental data. Regarding the enthalpy of fusion of the binary VW, both PBE and LDA predict larger values than the CALPHAD value. The volume changes at the melting point predicted from PBE

TABLE II. Calculated $T = 0$ K properties, lattice constant a_0, and bulk modulus B_0, and melting properties, melting temperature T^m, enthalpy of fusion ΔH^m, entropy of fusion ΔS^m, and volume change ΔV^m at the melting temperature, for GGA-PBE and LDA. Melting temperatures calculated without the electronic contribution $T^m_{\mathrm{no-ele}}$ are also included. Moreover, the experimental or CALPHAD values are included. As it is rather difficult to experimentally measure ΔV^m, such values are rare or nonexistent. We have therefore added values (shown in brackets) obtained by $V^m_{\mathrm{liquid}} - V^m_{\mathrm{solid}}$, where V^m_{liquid} and V^m_{solid} are the absolute experimental volumes of the liquid and solid at the experimental melting point.

	V			VW			W		
	GGA	Experiment	LDA	GGA	CALPHAD	LDA	GGA	Experiment	LDA
a_0 (Å)	2.999	3.027[a]/3.024[b]	2.930	3.093	3.094[g]	3.040	3.182	3.165[i]	3.138
B_0 (GPa)	183	157[b]	211	245	–	275	305	314[j]	336
T^m (K)	2140	2172[a]/2183[c]/2201[d]	2230	2704	2780[h]	2877	3349	3687±7[k,l]	3804
$T^m_{\mathrm{no-ele}}$ (K)	2161	–	2252	2803	–	2967	3527	–	3962
ΔH^m (kJ/mol)	24.31	26.5[c]/23.02[d]/17.32[e]	26.3	37.92	33.63[h]	39.78	44.31	50.34[l]/45.4[m]/61.4[n]	44.66
ΔH^m (meV/atom)	251.9	274.7[c]/238.6[d]/179.5[e]	272.6	393.0	348.6[h]	412.3	459.3	521.7[l]/470.5[m]/636.4[n]	462.8
ΔS^m [J/(mol K)]	11.36	12.14[c]/10.46[d]	11.79	14.02	12.09[h]	13.83	13.34	13.65[l]/12.31[n]	11.74
ΔS^m (k_B/atom)	1.37	1.46[c]/1.26[d]	1.42	1.69	1.45[h]	1.66	1.60	1.64[l]/1.48[n]	1.41
ΔV^m (Å^3/atom)	0.63	0.57[a]/0.7[c]	0.54	0.68	0.80[h]	0.66	0.98	(1.35–1.81)	0.87
V^m_{liquid} (Å^3/atom)	15.16	15.51[a]/15.49[c]/14.75[f]	14.03	16.67	16.86[h]	15.78	18.46	18.31[p]/18.65[q]/18.77[r]	17.72
V^m_{solid} (Å^3/atom)	14.53	14.94[a]/14.79[c]	13.49	15.99	16.06[h]	15.12	17.48	16.94[o]/16.96[s]	16.85

[a]Reference [69]; [b]Reference [73]; [c]Reference [74]; [d]Reference [8]; [e]Reference [9]; [f]Reference [75]; [g]Reference [70]; [h]Reference [47]; [i]Reference [76]; [j]Reference [77]; [k]Reference [78]; [l]Reference [13]; [m]Reference [14]; [n]Reference [15]; [o]Reference [79]; [p]Reference [80]; [q]Reference [81]; [r]Reference [82]; [s]Reference [83].

(0.68 Å^3/atom) and LDA (0.66 Å^3/atom) are similar, but both are smaller than the CALPHAD value (0.80 Å^3/atom). This trend is consistent with that for W as shown in Table II. Note that there are generally no data about the volume change from the solid to the liquid at the melting temperature in the database. But they can be important for defining the phase boundary in the phase diagram. With our approach these data can be easily accessed.

As discussed in Sec. II C, both the solid and liquid VW binary can be considered fully disordered at elevated temperatures (Fig. 1). Consequently, the ideal mixing approximation becomes applicable. By employing the ideal mixing approx-

imation and utilizing the Gibbs energy values for V and W obtained from PBE and LDA, the solidus and liquidus lines are easily determined as depicted by the dotted lines in Fig. 5. The over/under binding tendencies inherent in LDA/PBE are evident in these lines, with LDA data shifting upwards and PBE data shifting downwards.

D. Analysis of the electronic contribution

As mentioned in Sec. III B, the electronic contribution can significantly shift the predicted melting temperature for W
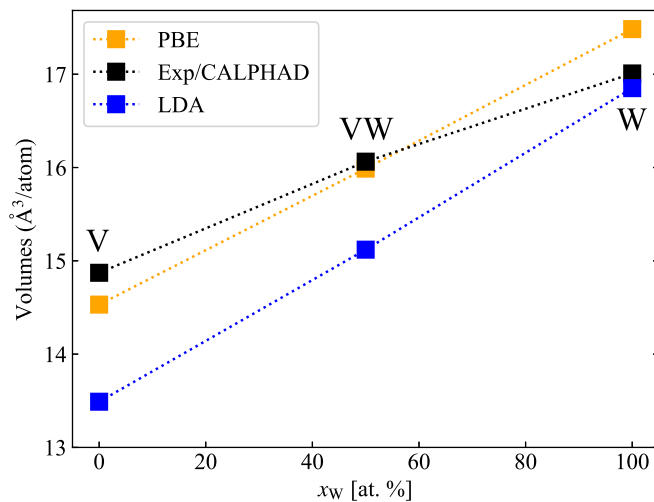

FIG. 6. Volumes of solid V, VW, and W at the corresponding melting temperature from PBE (orange), experiment (CALPHAD for VW) (black) and LDA (blue). The dotted lines are a guide to the eye and emphasize the linear trend.
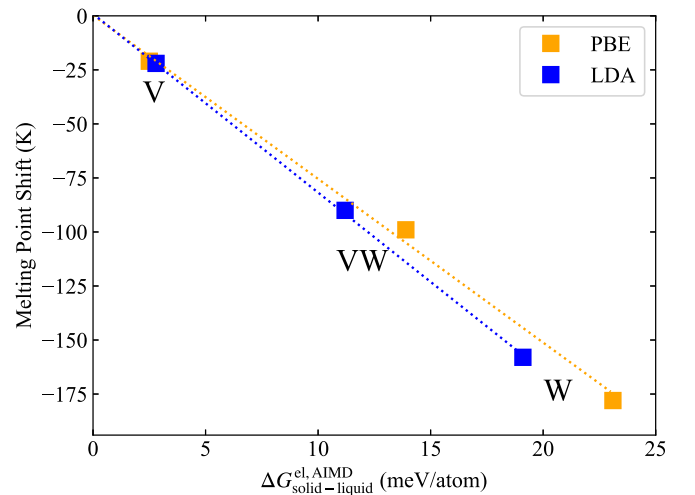

FIG. 7. Computed shift in the melting point induced by the electronic contribution to the Gibbs energy difference between the solid and liquid using PBE (orange) and LDA (blue). The electronic Gibbs energy difference $\Delta G^{\mathrm{el,AIMD}}_{\mathrm{solid-liquid}}$ is obtained by $(G^{\mathrm{el}}_{\mathrm{solid}}-G^{\mathrm{no-el}}_{\mathrm{solid}}) - (G^{\mathrm{el}}_{\mathrm{liquid}}-G^{\mathrm{no-el}}_{\mathrm{liquid}})$ at the corresponding melting point.
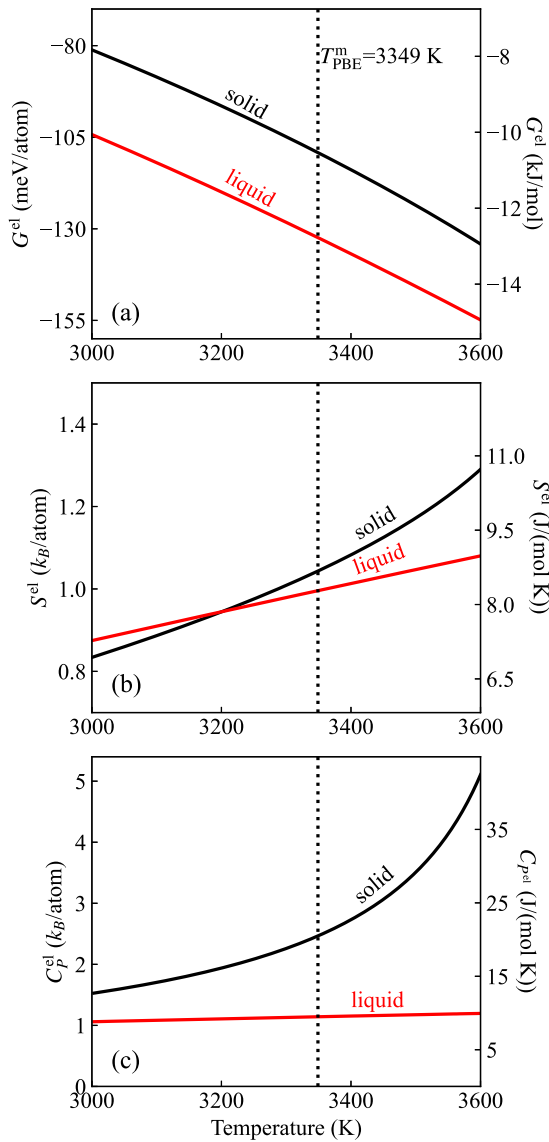
FIG. 8. Electronic contribution to (a) Gibbs energy, G^{el}; (b) entropy, S^{el}; and (c) heat capacity, C_P^{el}, for bcc and liquid W from PBE calculations.

because the electronic contribution lowers the liquid Gibbs energy more than it lowers the solid one [see Fig. 8(a)]. With the PBE functional the Gibbs energy difference between solid and liquid W due to the electronic contribution, $\Delta G_{\text{solid-liquid}}^{\text{el,AIMD}}$ ("AIMD" indicates *ab initio* MD simulation), is 23.1 meV/atom. It triggers a melting point shift of -178 K (see Fig. 7). For V and binary VW, the Gibbs energy differences are 2.5 and 13.9 meV/atom, respectively. They lead to a melting point shift of -21 K for V and -99 K for VW. These results reveal that the electronic contribution has a strong impact on W but a much smaller one for V. For binary VW the electronic contribution falls midway between V and W. Thus, it should be carefully taken into account for predicting the melting properties of binary VW. As shown in Fig. 7, the melting point shift has an approximately linear relationship with the electronic Gibbs energy difference for both PBE and LDA calculations. The slopes from PBE and LDA data are

rather close. As the entropy of fusion ΔS^m corresponds to $\Delta G_{\text{solid-liquid}}/\Delta T^m$, it indicates that the three systems have a constant/similar entropy of fusion. We discuss this further in Sec. III G in comparison to fcc elements.

It should be stressed that the stronger electronic Gibbs energy contribution in the liquid phase as compared to the solid phase [see Fig. 8(a)] does not necessarily mean that the derivative quantities show the same trend. The electronic entropy of solid and liquid, i.e., the first derivative of the electronic Gibbs energy with respect to temperature, turns out to be similar for W at the melting point with only a small difference of ~ 0.04 kB/atom [see Fig. 8(b)]. A small electronic entropy difference between solid and liquid is also observed for V and VW. Moving on to the electronic heat capacity, i.e., the second derivative of the Gibbs energy, we see a markedly different behavior than for the electronic Gibbs energy of W. For C_P, the electronic contribution is much stronger for the solid than for the liquid [see Fig. 8(c)], which is in qualitative contrast to the electronic Gibbs energy. For VW we observe the same trend as for W. But for V the electronic contribution to the difference in solid and liquid C_P at the predicted melting point is relatively small, which is consistent with the difference for the electronic Gibbs energy of V.

The impact of the electronic contribution on the Gibbs energy of the solid and liquid can be traced back to the respective electronic DOS and the corresponding DOS difference at the Fermi level. A key point to consider here is the electron-vibration coupling which generally leads to a strong smoothening of the electronic DOS at high temperatures [25,32,84]. It is therefore essential to analyze the electronic DOS computed from *ab initio* MD simulations at relevant temperatures. Moreover, to relate the DOS difference between the solid and liquid to the electronic Gibbs energy difference, consistent equilibrium volumes of the solid and liquid at the corresponding temperature should be used.

Figure 9 shows the computed electronic DOS's of the solid and liquid V, W, and binary VW from *ab initio* MD at temperatures close to the experimental/CALPHAD melting points and at the consistent equilibrium volumes. We focus on results obtained from PBE. For V, the high temperature DOS of the liquid (red line) at the Fermi level is slightly above that of the solid (blue line) with a difference of $\Delta N_{\text{liquid-solid}}(E_F) = 0.07$ states/(eV atom) [see Fig. 9(a) and Table III], which results in the aforementioned electronic Gibbs energy difference of 2.5 meV/atom. For binary VW, the presence of W introduces more valence electrons in the DOS and shifts the Fermi level to higher energies as compared to V [see Fig. 9(b)]. In this case, a small gap opens between the solid and liquid DOS at the Fermi level with a difference of 0.22 states/(eV atom), which corresponds to the electronic Gibbs energy difference of 13.9 meV/atom in Fig. 7.

For pure W, the Fermi level is pushed even further to higher energies due to more valence electrons. As a consequence, the Fermi level falls into a pronounced minimum in the solid DOS [see the blue line in Fig. 9(c)]. Having the Fermi level in a pseudo valley indicates that the chemical bond in bcc W retains a strong covalent character even at high temperatures. Compared to the DOS of bcc W, the DOS of liquid W is more smeared out due to a higher degree of disorder. The difference in the solid and liquid DOS at the Fermi level is
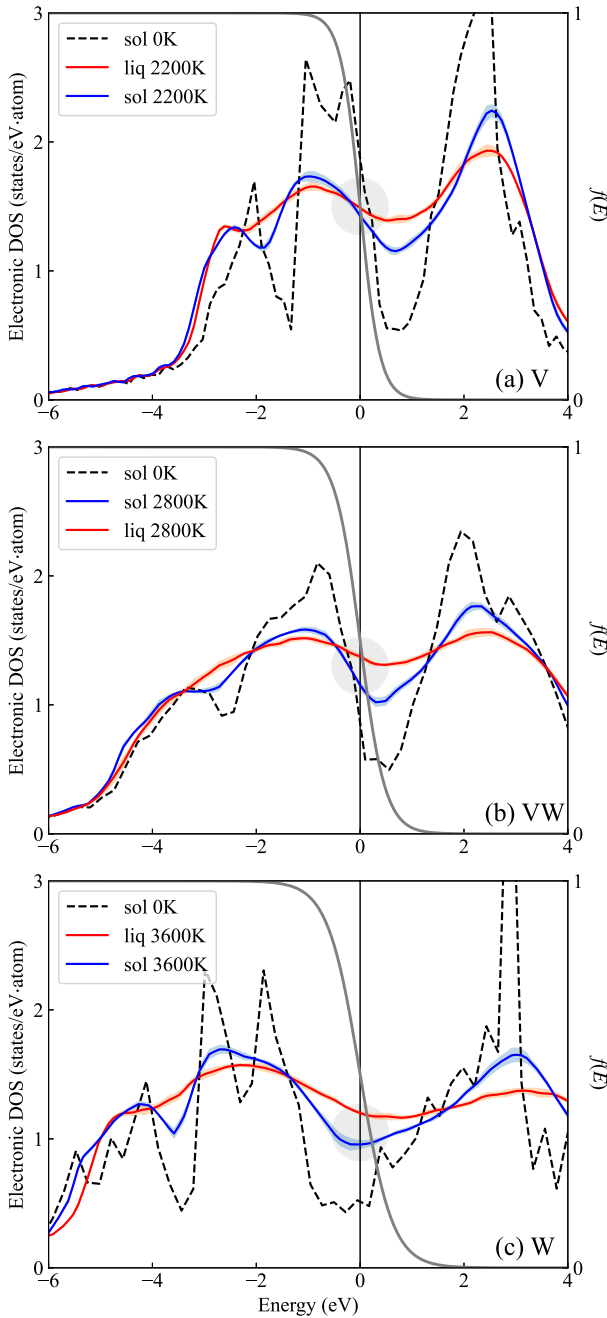
FIG. 9. The electronic DOS of the solid and liquid phase at their respective equilibrium volumes for (a) V at 2200 K, (b) VW at 2800 K, and (c) W at 3600 K. The black dashed lines give the electronic DOS for the ideal static lattice with the electronic temperature equal to the selected MD temperature. The blue and red lines are the mean solid and liquid DOS's from a statistically converged set of uncorrelated AIMD snapshots. The standard deviation resulting from the different snapshots is shown by the blue/red shaded areas. The gray lines indicate the Fermi-Dirac occupation $f(E)$ at the corresponding temperature. All DOS's are computed using PBE.

0.25 states/(eV atom) as shown in Fig. 9(c). Although this difference is similar as that in VW, it triggers a larger electronic Gibbs energy difference of 23.1 meV/atom in W. This can be explained by two factors—the relatively stronger Fermi

TABLE III. The electronic DOS at the Fermi level for solid, $N_{\text{solid}}(E_F)$, and liquid, $N_{\text{liquid}}(E_F)$, the DOS difference, $\Delta N_{\text{liquid}-\text{solid}}(E_F)$, the electronic Gibbs energy difference based on the Sommerfeld approximation, $\Delta G^{\text{el,SOM}}_{\text{solid}-\text{liquid}}$, and our calculated difference from AIMD, $\Delta G^{\text{el,AIMD}}_{\text{solid}-\text{liquid}}$. The DOS values correspond to the mean of 10 snapshots from AIMD simulations at 2200 K for V, 2800 K for VW, and 3600 K for W [cf. Figs. 9(a)–9(c)].

	V	VW	W
$N_{\text{solid}}(E_F)$ (states/eV atom)	1.42	1.15	0.95
$N_{\text{liquid}}(E_F)$ (states/eV atom)	1.49	1.37	1.2
$\Delta N_{\text{liquid}-\text{solid}}(E_F)$ (states/eV atom)	0.07	0.22	0.25
$\Delta G^{\text{el,SOM}}_{\text{solid}-\text{liquid}}$ (meV/atom)	4.1	21.1	39.6
$\Delta G^{\text{el,AIMD}}_{\text{solid}-\text{liquid}}$ (meV/atom)	2.5	13.9	23.1

broadening in W due to its higher melting point than that of VW, as shown by the solid gray lines in Fig. 9, and the larger difference between the solid and liquid DOS's (red and blue lines) in W around the Fermi level (gray shaded region).

Actually, most transition metals with high melting points, such as V, do not show a large difference in the DOS of the solid and liquid at the Fermi level [19]. What makes W special is its half-filled electron d-band in the bcc lattice structure. A similar behavior was observed earlier for the other group VI elements bcc Mo [17] and Cr [24].

E. Heat capacity of solid and liquid W

The heat capacity is important in thermodynamic modeling, particularly of phase stability and phase diagrams. It is thus critical to accurately estimate different physical contributions to the heat capacity. As the electronic contribution has the largest impact on W among the three investigated systems, in the following the heat capacity of W is discussed as an example.

Figure 10(a) shows the quasiharmonic (qh), anharmonic (ah), and static electronic (el,static) contributions, and the contribution from electron-vibration coupling (el-vib) to the isobaric heat capacity C_P. Figure 10(b) shows the vibrational (vib) and electronic contributions (el,static + el-vib) to C_P and to the isochoric heat capacity C_V for liquid W. The orange regions in both figures mark the electronic contribution including its coupling to atomic vibrations. The impact is large for both solid and liquid. In Fig. 10(c) we compare our calculated C_P for the solid with the liquid one, and with experimental data from the literature. The calculated C_P for bcc W (black solid line) lies close to the experimental data (red dotted line below the melting point), only when the electronic contribution is fully taken into account. Not taking the electronic contribution (black dashed line) into account clearly increases the deviation from the experimental data. A similar conclusion can also be made for the liquid C_P, where our calculations including the electronic contribution (blue solid lines) fall closer to most of the experimental data points (red symbols above melting point).

The heat capacity C_P of a liquid is often assumed to be temperature independent, as shown by the red dotted line above melting point. However, our calculated C_P for liquid W decreases within the investigated temperature range
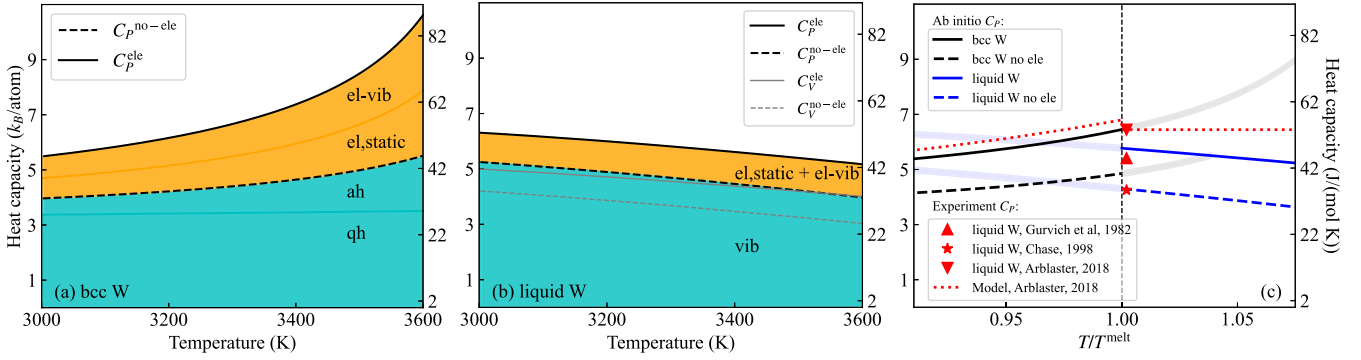
FIG. 10. Computed isobaric heat capacity C_P as a function of temperature for (a) bcc W and (b) liquid W. The individual contributions are indicated (see text). C^{el} represents the data fully taking into account the electronic contributions (both static and coupling to vibrations), while C^{no-el} stands for the data without any electronic contribution. For liquid W, we also include the isochoric heat capacity C_V, with and without electronic contribution. (c) C_P of bcc and liquid W in comparison to experiment/CALPHAD. The faded lines indicate the metastable regime of the solid above the melting point and of the liquid below the melting point. The red dotted lines represent the analytical model from Ref. [13] based on experimental data with temperatures ranging from 253 K to 3680 K [91–97]. The red up-triangle, star and down-triangle mark selected liquid heat capacities from different assessments [11–13] at the melting point. In (c), both our DFT data and the experimental data are plotted on a homologous temperature scale, i.e., they are normalized by the corresponding calculated/experimental melting temperatures. All shown DFT data correspond to PBE.

3000–3600 K from 6.31 to 5.17 k_B/atom and C_V from 4.99 to 4.0 k_B/atom [Fig. 10(b)]. The decreasing behavior of the heat capacity for liquid W was observed for both PBE and LDA calculations. This trend qualitatively agrees with a recent CALPHAD assessment for liquid W [18]. In fact, for many liquids, literature data indicates that the heat capacity decreases with temperature [85–87]. For instance, Forsblom and Grimvall showed a decreasing C_P from the melting point T^m to 2 times T^m in liquid Al using MD simulations with empirical potentials [88]. The reason of a decreasing heat capacity in liquids has been attributed to the increasing loss of two transverse modes in the liquid [88–90]. Experiments also indicate a decreasing C_P with temperature [85]. However, measuring the heat capacity of a liquid is in general very challenging. The enthalpy $H(T)$ is measured in the first place and C_P is obtained by computing the first derivative $\frac{\partial H}{\partial T}$. Thus, the experimental accuracy is often insufficient to resolve deviations from a linear relationship between H and T. Empirical potential simulations can help, but their accuracy strongly depends on the quality of the potential. The TOR-TILD method provides instead the possibility to obtain an accurate heat capacity of the liquid phase fully from *ab initio*.

F. Limitations of the Sommerfeld approximation

The Sommerfeld model [21,22] has been widely used to parametrize the electronic free energy and electronic heat capacity in thermodynamic modeling approaches, especially in the CALPHAD community [3]. The SOM approximation to the electronic free energy assumes a quadratic temperature dependence and reads as

$$F_{SOM}^{el} = -\frac{1}{6}\pi^2 k_B^2 T^2 N(E_F), \qquad (1)$$

where the value of the DOS at the Fermi level $N(E_F)$ is the only input parameter and therefore crucially affects

the computed electronic free energy F_{SOM}^{el}. As shown in Figs. 9(a)–9(c), the DOS's of the ideal lattice (black dashed lines) for V, VW, and W are significantly different from those of the solid computed at high temperatures (blue lines). Thus, using the DOS of the ideal static lattice to compute F_{SOM}^{el} would introduce a huge error. We therefore use our calculated high-temperature DOS at the corresponding equilibrium volume and compute the electronic Gibbs energy differences between the solid and liquid based on the Sommerfeld approximation in Eq. (1). The computed Gibbs energy differences, $\Delta G_{solid-liquid}^{el,SOM}$, are respectively 4.1 meV/atom for V, 21.1 meV/atom for VW, and 39.6 meV/atom for W (see Table III). Even though the high-temperature DOS's used here for both solid and liquid fully include the impact of atomic vibrations and electron-vibration coupling, they are still quantitatively different from our direct *ab initio* MD results (2.5 meV/atom for V, 13.9 meV/atom for VW, and 23.1 meV/atom for W, see Table III).

The electronic heat capacity is related to the second derivative of the electronic free energy with respect to temperature. Therefore, the error introduced in the electronic Gibbs energy due to the simplification of the Sommerfeld approximation can be significantly enlarged in the prediction of the electronic heat capacity. Based on Eq. (1) the electronic contribution to the isochoric heat capacity in the Sommerfeld approximation can be obtained by

$$C_{V,SOM}^{el} = \frac{1}{3}\pi^2 k_B^2 T N(E_F). \qquad (2)$$

Then the electronic heat capacity difference between solid and liquid can be accessed by

$$\Delta C_{V,SOM}^{el} = \frac{1}{3}\pi^2 k_B^2 T^m [N_{liquid}(E_F) - N_{solid}(E_F)], \qquad (3)$$

where the DOS's are computed at the corresponding equilibrium volumes. Similarly to our previous discussions on the electronic Gibbs energy difference, the difference in electronic heat capacity also varies significantly depending on
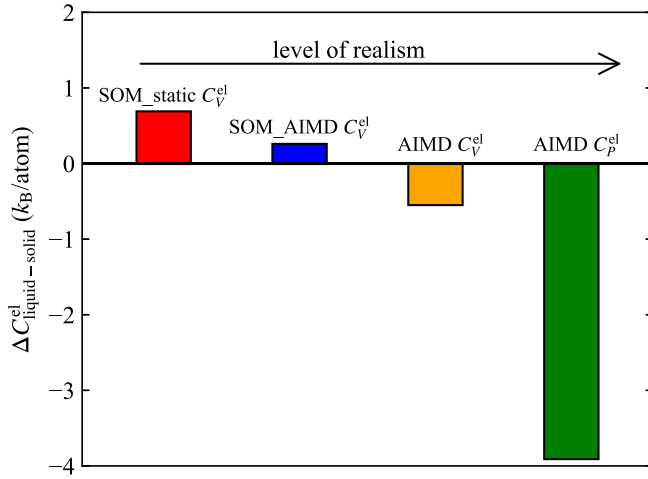
FIG. 11. Electronic contribution to the heat capacity difference between solid and liquid W from the SOM approximation and from AIMD. "SOM_static C_V^{el}" indicates the value obtained by the Sommerfeld approoaximation using the solid DOS of the ideal static lattice [the black dashed line in Fig. 9(c)], "SOM_AIMD C_V^{el}" the value obtained by the Sommerfeld approximation using the DOS of the solid at high temperatures [the blue line in Fig. 9(c)] calculated from AIMD, "AIMD C_V^{el}" and "AIMD C_P^{el}" the AIMD values at constant volume and pressure, respectively.

the DOS used. For example, keeping the high-temperature DOS of the liquid fixed, when the DOS of the solid changes from that of the static lattice to the high-temperature DOS, the electronic heat capacity difference changes from 0.69 k_B/atom to 0.26 k_B/atom (see the red and blue bars in Fig. 11).

In Ref. [19] Grimvall estimated an electronic heat capacity difference of 0.5 k_B/atom using the Sommerfeld approximation. It lies in between the two Sommerfeld evaluations considered here (0.69 and 0.26 k_B/atom). The small discrepancy can be explained as follows. In his approximation [19] the DOS of solid W was derived from a calculation

for the ideal static lattice using the full-potential linearized augmented-plane-wave method [23]. Further, the DOS of liquid W was estimated from a comparison with the calculated DOS for bcc and liquid Cr [24] and Mo [17].

However, our full *ab initio* MD approach gives qualitatively different results for W. At 3600 K the difference is $-0.55\ k_B$/atom as shown by the orange bar in Fig. 11. The negative sign indicates that the electronic heat capacity of the solid is larger than that of the liquid. When going to C_P^{el} corresponding to the typical experimental conditions, the difference between solid and liquid is more prominent with a value of $-3.9\ k_B$/atom at 3600 K (the green bar in Fig. 11). The qualitative difference between the results from the Sommerfeld model (positive values) and those from our *ab initio* MD calculations (negative values) demonstrates the limitation of applying the Sommerfeld model to predict the electronic heat capacity difference between the solid and liquid.

G. Enthalpy and entropy of fusion for bcc and fcc

Based on experimental data, Sawamura [98] derived an empirical relationship between the enthalpy of fusion and the melting point. Both bcc and fcc metals show a linear relationship with the same slope but with different offsets. Sawamura [98] further stated that, even though V has a bcc lattice, it rather falls onto the relationship of the fcc metals. We utilize the *ab initio* results from the present study for the bcc metals V, W, and the binary VW alloy and from our previous works for the fcc metals Al, Cu, Ni [31,32] to scrutinize the empirical prediction.

Figure 12(a) shows the PBE, LDA, and experimental enthalpy of fusions for various systems as a function of the consistent melting point. For the fcc systems, we indeed observe a linear relationship (see the solid line labeled "fcc"), in which the theoretical and experimental data are very consistent. However, the experimentally derived suggestion that bcc V falls onto this fcc line cannot be confirmed with our calculated data. Instead, the *ab initio*–derived enthalpy of fusion of bcc V lies above the fcc line. This finding is also
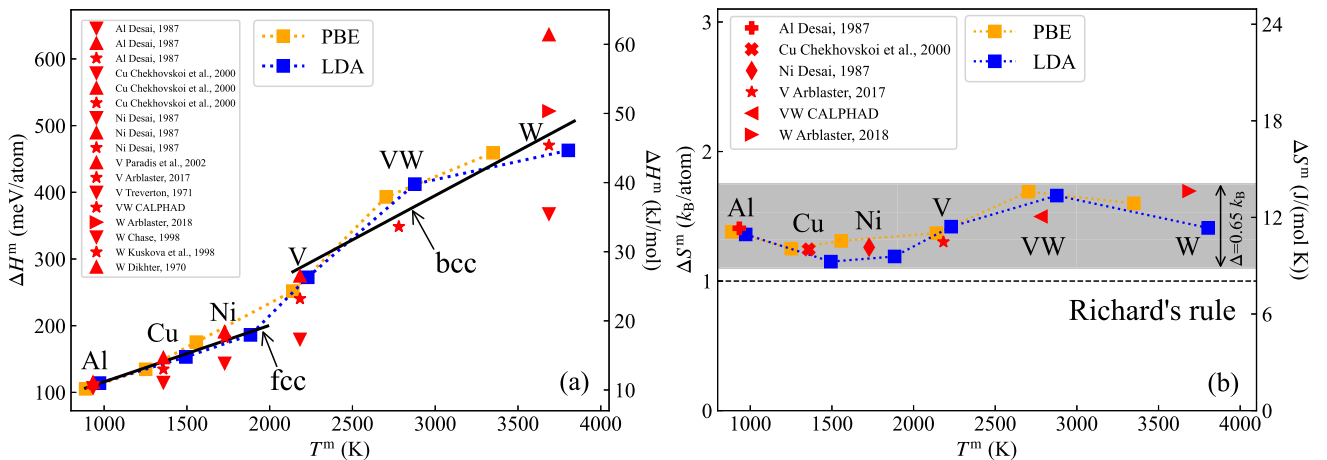

FIG. 12. (a) Enthalpy and (b) entropy of fusion computed from PBE (orange) and LDA (blue) as a function of the corresponding computed melting temperature. The red symbols are from experiment [8,9,12–15,74,99–101] or derived from Gibbs energies extracted with the CALPHAD method. In (a), the black lines are linear fits to the DFT data (both PBE and LDA) for fcc and bcc metals. In (b), the dashed line corresponds to the value given by Richard's rule.
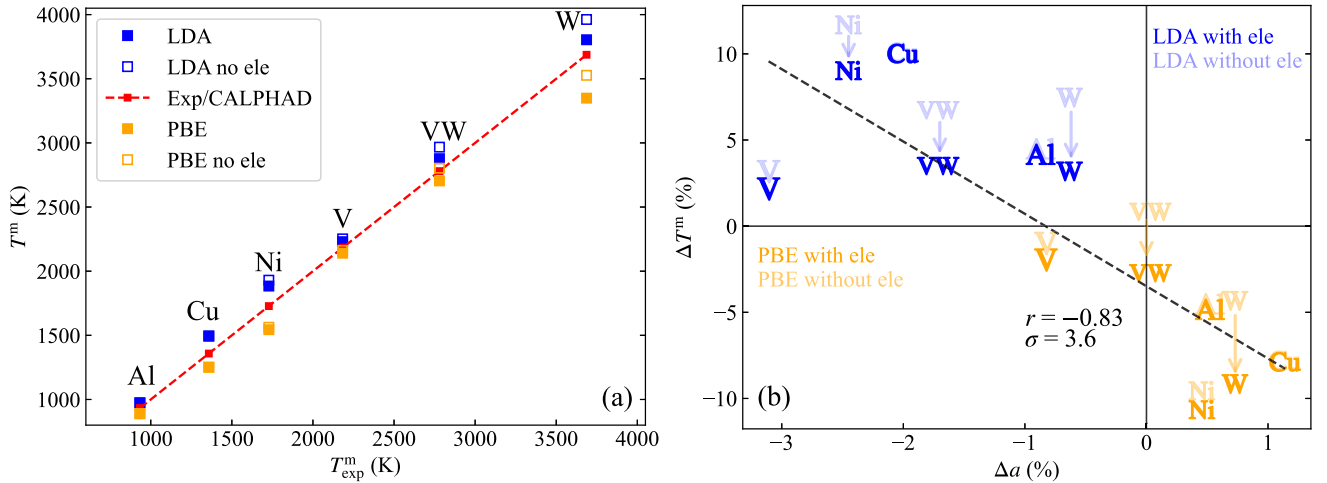
FIG. 13. (a) Comparison between computed (PBE and LDA) and experimental/CALPHAD melting points of Al, Cu, Ni, V, W, and binary VW. The empty squares represent data without taking into account the electronic free-energy contribution. Note that PBE and LDA provide a lower and upper bound for all experimental melting points. (b) Correlation between the deviation from experiment for the lattice constants Δa at $T = 0$ K and the melting temperatures ΔT^m. Data with and without taking into account the electronic free-energy contribution are provided. Arrows indicate the change due to the electronic contribution for the systems with a strong impact. The black dashed line is a linear fit of the data with the electronic contribution. The Pearson correlation coefficient r and the standard deviation σ of the fitted data are given in (b).

supported by two experimental measurements from literature. The previous suggestion on bcc V may be a false consequence of experimental scatter.

Figure 12(a) further reveals that the enthalpy of fusions of all the investigated bcc systems lie above the fcc line. A linear fit of these data points is obtained and shown by the line labeled "bcc." However, the fit is not as good as for the fcc elements, and further simulations are required to elaborate the relationship. Nevertheless, with the highly accurate theoretical data from the present work, one can see the tremendous benefit in complimenting the strongly scattered experimental values, e.g., from 35 to 61 kJ/mol for W.

For the entropy of fusion, a simple empirical rule, Richard's rule, suggests that the entropy of fusion of most materials is $\approx 1\ k_B$/atom [19]. Figure 12(b) shows the PBE, LDA, and experimental entropy of fusions. They confirm the approximately constant value of the entropy of fusion regardless of the melting temperature. The mean values from PBE and LDA are $\approx 1.43\ k_B$/atom and $\approx 1.36\ k_B$/atom, respectively. These values are close to the mean value (1.36 k_B/atom) obtained from experimental data. Our computed DFT results and the experimental data from literature fall within the gray belt between 1.1 and 1.75 k_B/atom. Therefore, the Richard's rule can be considered as a lower bound of "true" entropy of fusion for the investigated systems.

H. Performance of GGA and LDA in predicting melting properties

The performance of various exchange-correlation functionals has been systematically evaluated on several $T = 0$ K material properties, such as lattice constants, bulk moduli, or elastic constants [65]. However, the functionals have been rarely tested on melting properties of materials due to the computational costs involved in *ab initio* MD simulations.

The efficiency of the TOR-TILD method could allow us to fill the research gap in this respect.

Figure 13(a) gives our calculated melting points from both PBE and LDA as a function of the experimental melting temperature for bcc V, W, VW binary, fcc Al, Cu, and Ni [31,32]. This plot demonstrates the applicability of the concept of the *ab initio* confidence interval to all investigated systems, i.e., the experimental melting points fall in between the PBE and LDA predictions. Figure 13(b) indicates that the under(over)estimation of the melting points by PBE (LDA) is, in general, correlated with the deviations in the computed equilibrium lattice constants from the experimental ones. The Pearson correlation coefficient r is used to measure the strength of the linear correlation. A value of -0.83 is obtained for the data taking into account the electronic contribution, indicating a strong anticorrelation. A linear fit for these data is given by the black dashed line in Fig. 13(b), with a standard deviation of 3.6%. The reason that bcc V from PBE falls out of the bottom-right box ($\Delta a > 0$ and $\Delta T^m < 0$) is that the PBE also underestimates the equilibrium lattice constant as LDA does, but its prediction is much closer to experimental data. For the binary VW a similar performance of PBE and LDA for predicting the equilibrium lattice constant as for V is observed likely due to the participation of V. As the PBE predicted equilibrium lattice constant for the binary VW is almost overlapping with the experimental data (see Table II), the PBE prediction for binary VW in Fig. 13(b) falls on the border line of $\Delta a = 0$.

IV. CONCLUSIONS

A key insight of the present work is the strong impact of electronic excitations on the melting point of W. Including properly electronic excitations, and very importantly their coupling to atomic vibrations, into the finite-temperature *ab initio* modeling reduces the melting point by 178 K. The

electrons also affect the heat capacity of W, both in its solid and liquid phase, but with a different intensity in each phase. The physical reason for the difference between the solid and liquid phase can be traced back to and understood in terms of the electronic density of states in the vicinity of the Fermi level. The electronic impact emanates to the VW binary and can be expected to affect W containing alloys in general, for example, the recently intensively investigated class of refractory high-entropy alloys. Thermodynamic modeling of melting properties of such alloys should therefore integrate the electronic free energies. Crucially, in doing so, one should be very cautious about the Sommerfeld approximation, which has been shown here to have severe limitations.

The heat capacity of W in the liquid phase, including the contribution of electronic excitations, shows a decreasing temperature dependence. Such a dependence was observed earlier with empirical potentials and experimentally but could be manifested only now with finite-temperature *ab initio* simulations. Supportively, the decreasing temperature dependence of the liquid heat capacity in W is observed for both employed exchange-correlation functionals, the (LDA and the generalized gradient approximation (GGA-PBE). The here utilized methodology thus fills a gap by complementing the challenging high-temperature experiments which often show strong scatter in the measured heat capacity data.

When considering absolute quantities such as the melting temperature one has to be aware of potentially larger discrepancies. For W, the predicted melting temperature is below the experimental value by more than 300 K when the GGA-PBE exchange-correlation functional is employed. The confidence in such calculations can be increased by additional calculations with a second exchange-correlation functional, specifically the LDA. This approach provides a lower and an upper bound to the experimental data. These bounds function as an *ab initio* confidence interval, since the confidence in predicting experiment is larger when the bounds are narrower. The present results for V, W, and VW—together with previous results for Al, Cu, and Ni—show that the confidence-interval concept applies to the melting points of all these elements.

To facilitate future computations, a part of the TOR-TILD methodology has been implemented as an independent workflow in pyiron [102]—an integrated development environment for computational material science—and can be applied with arbitrary empirical potentials using the interface method [103]. The corresponding pyiron notebook for the present work with respect to the interface method is available [104].

[1] N. Saunders, A. P. Miodownik, and A. T. Dinsdale, Calphad **12**, 351 (1988).

[2] M. Hillert, *Phase Equilibria, Phase Diagrams and Phase Transformations: Their Thermodynamic Basis* (Cambridge University Press, Cambridge, UK, 2007).

[3] L. Kaufman and H. Bernstein, *Computer Calculation of Phase Diagrams* (Academic Press, New York, 1970).

[4] O. Senkov, G. Wilks, J. Scott, and D. Miracle, Intermetallics **19**, 698 (2011).

[5] O. Senkov, G. Wilks, D. Miracle, C. Chuang, and P. Liaw, Intermetallics **18**, 1758 (2010).

[6] B. Grabowski, Y. Ikeda, P. Srinivasan, F. Körmann, C. Freysoldt, A. I. Duff, A. Shapeev, and J. Neugebauer, npj Comput. Mater. **5**, 80 (2019).

[7] O. Senkov, S. Gorsse, and D. Miracle, Acta Mater. **175**, 394 (2019).

[8] J. W. Arblaster, J. Phase Equilib. Diffus. **38**, 51 (2017).

[9] J. A. Treverton and J. L. Margrave, J. Chem. Thermodyn. **3**, 473 (1971).

[10] U. Seydel, H. Bauhof, W. Fucke, and H. Wadle, High Temp. High Press. **11**, 635 (1979).

[11] L. V. Gurvich, I. V. Veits, V. A. Medvedev, G. A. Khachkuruzov, V. S. Yungman, and G. A. Bergman, *Thermo-dynamic Properties of Individual Substances*, edited by V. P. Glushko (Izd. Nauka, Moscow, 1982).

[12] M. W. Chase Jr., J. Phys. Chem. Ref. Data, Monongr. **9**, 1925 (1998).

[13] J. W. Arblaster, J. Phase Equilib. Diffus. **39**, 891 (2018).

[14] N. I. Kuskova, S. I. Tkachenko, and S. V. Koval, Int. J. Thermophys. **19**, 341 (1998).

[15] I. Ya. Dikhter and S. V. Lebedev, High Temp. High Press. **2**, 55 (1970).

[16] B. Fultz, Prog. Mater. Sci. **55**, 247 (2010).

[17] J. A. Moriarty, Phys. Rev. B **49**, 12431 (1994).

[18] Z. He and M. Selleby, Mater. Chem. Phys. **276**, 125445 (2022).

[19] G. Grimvall, *Thermophysical Properties of Materials* (Elsevier, Amsterdam, 1999).

[20] G. Grimvall, M. Thiessen, and A. F. Guillermet, Phys. Rev. B **36**, 7816 (1987).

[21] N. W. Ashcroft and N. D. Mermin, in *Solid State Physics*, 1st ed. (Harcourt College, Orlando, 1976), Chap. 2, pp. 29–56.

[22] C. Wolverton and A. Zunger, Phys. Rev. B **52**, 8813 (1995).

[23] H. J. F. Jansen and A. J. Freeman, Phys. Rev. B **30**, 561 (1984).

[24] W. Jank, Ch. Hausleitner, and J. Hafner, J. Phys.: Condens. Matter **3**, 4477 (1991).

[25] X. Zhang, B. Grabowski, F. Körmann, C. Freysoldt, and J. Neugebauer, Phys. Rev. B **95**, 165126 (2017).

[26] O. Sugino and R. Car, Phys. Rev. Lett. **74**, 1823 (1995).

[27] G. A. de Wijs, G. Kresse, and M. J. Gillan, Phys. Rev. B **57**, 8223 (1998).

[28] D. Alfè, M. J. Gillan, and G. D. Price, Nature (Lond) **401**, 462 (1999).

[29] D. Alfè, G. D. Price, and M. J. Gillan, Phys. Rev. B **65**, 165118 (2002).

[30] L. Vočadlo and D. Alfè, Phys. Rev. B **65**, 214105 (2002).

[31] L.-F. Zhu, B. Grabowski, and J. Neugebauer, Phys. Rev. B **96**, 224202 (2017).

[32] L.-F. Zhu, F. Körmann, A. V. Ruban, J. Neugebauer, and B. Grabowski, Phys. Rev. B **101**, 144108 (2020).

[33] L. G. Wang, A. van de Walle, and D. Alfè, Phys. Rev. B **84**, 092102 (2011).

[34] Y. Zhang, Y. Tan, H. Y. Geng, N. P. Salke, Z. Gao, J. Li, T. Sekine, Q. Wang, E. Greenberg, V. B. Prakapenka, and J.-F. Lin, Phys. Rev. B **102**, 214104 (2020).

[35] T. Zhang, S. Wang, H. Song, S. Duan, and H. Liu, J. Appl. Phys. **126**, 205901 (2019).

[36] B. Grabowski, T. Hickel, and J. Neugebauer, Phys. Rev. B **76**, 024309 (2007).

[37] B. Grabowski, L. Ismer, T. Hickel, and J. Neugebauer, Phys. Rev. B **79**, 134106 (2009).

[38] A. Glensk, B. Grabowski, T. Hickel, and J. Neugebauer, Phys. Rev. X **4**, 011018 (2014).

[39] A. I. Duff, T. Davey, D. Korbmacher, A. Glensk, B. Grabowski, J. Neugebauer, and M. W. Finnis, Phys. Rev. B **91**, 214311 (2015).

[40] Y. Zhou, P. Srinivasan, F. Körmann, B. Grabowski, R. Smith, P. Goddard, and A. I. Duff, Phys. Rev. B **105**, 214302 (2022).

[41] J. H. Jung, P. Srinivasan, A. Forslund, and B. Grabowski, npj Comput. Mater. **9**, 3 (2023).

[42] A. V. Shapeev, Multiscale Model. Simul. **14**, 1153 (2016).

[43] P. Srinivasan, A. Shapeev, J. Neugebauer, F. Körmann, and B. Grabowski, Phys. Rev. B **107**, 014301 (2023).

[44] A. Forslund, J. H. Jung, P. Srinivasan, and B. Grabowski, Phys. Rev. B **107**, 174309 (2023).

[45] A. I. Duff, M. W. Finnis, P. Maugis, B. J. Thijsse, and M. H. F. Sluiter, Comput. Phys. Commun. **196**, 439 (2015).

[46] J. R. Morris, C. Z. Wang, K. M. Ho, and C. T. Chan, Phys. Rev. B **49**, 3109 (1994).

[47] J. Bratberg, Z. Metallkd. **96**, 335 (2005).

[48] T. Kostiuchenko, A. V. Ruban, J. Neugebauer, A. Shapeev, and F. Körmann, Phys. Rev. Mater. **4**, 113802 (2020).

[49] A. Shapeev, Comput. Mater. Sci. **139**, 26 (2017).

[50] T. Kostiuchenko, F. Körmann, J. Neugebauer, and A. Shapeev, npj Comput. Mater. **5**, 55 (2019).

[51] A. Zunger, S.-H. Wei, L. G. Ferreira, and J. E. Bernard, Phys. Rev. Lett. **65**, 353 (1990).

[52] A. Fernández-Caballero, J. S. Wróbel, P. M. Mummery, and D. Nguyen-Manh, J. Phase Equilib. Diffus. **38**, 391 (2017).

[53] C. G. Schön, T. Duong, Y. Wang, and R. Arróyave, Acta Mater. **148**, 263 (2018).

[54] J. M. Cowley, Phys. Rev. **138**, A1384 (1965).

[55] N. Norman and B. E. Warren, J. Appl. Phys. **22**, 483 (1951).

[56] P. E. Blöchl, Phys. Rev. B **50**, 17953 (1994).

[57] G. Kresse and J. Hafner, Phys. Rev. B **47**, 558 (1993).

[58] G. Kresse and J. Hafner, Phys. Rev. B **49**, 14251 (1994).

[59] G. Kresse and J. Furthmuller, Comput. Mater. Sci. **6**, 15 (1996).

[60] G. Kresse and J. Furthmuller, Phys. Rev. B **54**, 11169 (1996).

[61] J. P. Perdew, K. Burke, and M. Ernzerhof, Phys. Rev. Lett. **77**, 3865 (1996).

[62] H. J. Monkhorst and J. D. Pack, Phys. Rev. B **13**, 5188 (1976).

[63] S. Plimpton, J. Comput. Phys. **117**, 1 (1995).

[64] J. O. Andersson, T. Helander, L. Höglund, P. F. Shi, and B. Sundman, Calphad **26**, 273 (2002).

[65] P. Haas, F. Tran, and P. Blaha, Phys. Rev. B **79**, 085104 (2009).

[66] K. Wang and R. Reeber, Mater. Sci. Eng. **R23**, 101 (1998).

[67] J. A. Weber, D. Benea, W. H. Appelt, H. Ceeh, W. Kreuzpaintner, M. Leitner, D. Vollhardt, C. Hugenschmidt, and L. Chioncel, Phys. Rev. B **95**, 075119 (2017).

[68] A. S. Belozerov, A. A. Katanin, and V. I. Anisimov, Phys. Rev. B **107**, 035116 (2023).

[69] Yu. M. Kozlovskii and S. V. Stankus, J. Phys.: Conf. Ser. **1677**, 012167 (2020).

[70] E. Rudy, Air Force Materials Lab., Wright-Patterson Air Force Base, OH, Rep. No. AFML-TR-65-2, part V, 122 (1969).

[71] V. V. Baron, Yu. V. Efimov, and E. M. Savitskii, Izv. Akad. Nauk SSSR, Otd. Tekh. Nauk., Metall. Top. **1**, 70 (1960) [Russ. Met. Fuels **1**, 45 (1960)].

[72] A. T. Dinsdale, Calphad **15**, 317 (1991).

[73] D. I. Bolef, R. E. Smith, and J. G. Miller, Phys. Rev. B **3**, 4100 (1971).

[74] P.-F. Paradis, T. Ishikawa, T. Aoyama, and S. Yoda, J. Chem. Thermodyn. **34**, 1929 (2002).

[75] M. A. Maurakh, Trans. Indian Inst. Met. **14**, 209 (1964).

[76] W. Parrish, Acta Cryst. **13**, 838 (1960).

[77] F. H. Featherston, *The Elastic Constants of Tantalum Tungsten and Molybdenum* (Naval Postgraduate School, Monterey, CA 1963).

[78] R. E. Bedford, G. Bonnier, H. Maas, and F. Pavese, Metrologia **33**, 133 (1996).

[79] L. S. Dubrovinsky and S. K. Saxena, Phys. Chem. Miner. **24**, 547 (1997).

[80] P. S. Martsenyuk, Yu. N. Ivashchenko, and V. N. Eremenko, High Temp. **12**, 1161 (1974) [Teplofiz. Vys. Temp. **12**, 1310 (1974)].

[81] U. Seydel and W. Kitzel, J. Phys. F: Met. Phys. **9**, L153 (1979).

[82] J. W. Shaner, G. R. Gathers, and C. Minichino, High Temp.-High Press. **8**, 425 (1976).

[83] A. P. Miiller and A. Cezairliyan, Int. J. Thermophys. **12**, 643 (1991).

[84] C. Asker, A. B. Belonoshko, A. S. Mikhaylushkin, and I. A. Abrikosov, Phys. Rev. B **77**, 220102(R) (2008).

[85] G. Grimvall, Phys. Scr. **11**, 381 (1975).

[86] D. C. Wallace, Phys. Rev. E **57**, 1717 (1998).

[87] A. R. Dexter and A. J. Matheson, Trans. Faraday Soc. **64**, 2632 (1968).

[88] M. Forsblom and G. Grimvall, Phys. Rev. B **72**, 132204 (2005).

[89] K. Trachenko, Phys. Rev. B **78**, 104201 (2008).

[90] K. Trachenko and V. V. Brazhkin, Rep. Prog. Phys. **79**, 016502 (2016).

[91] H. L. Bronson, H. M. Chisholm, and S. M. Dockerty, Can. J. Res. **8**, 282 (1933).

[92] D. A. Ditmars, High Temp. High Press. **11**, 615 (1979).

[93] E. D. West and S. Ishihara, Natl. Bur. Stand. Rep. **9803**, 80 (1968).

[94] A. Cezairliyan and J. L. McClure, J. Res. Nat. Bur. Stand. **75A**, 283 (1971).

[95] R. E. Taylor, Tans. ASME **100**, 330 (1978)

[96] F. Righini, J. Spišiak, G. C. Bussolino, and A. Rosso, in *Fifth International Symposium on Temperature and Thermal Measurement in Industry and Science (TEMPMEKO'93)* (Tech-Market, Prague, 1993), 360.

[97] E. Arpaci and M. G. Frohberg, Z. Metallkde. **75**, 614 (1984).

[98] H. Sawamura, Trans. JIM **13**, 225 (1972).

[99] P. D. Desai, Inter. J. Thermophys. **8**, 621 (1987).

[100] V. Ya. Chekhovskoi, V. D. Tarasov, and Yu. V. Gusev, High Temp. **38**, 394 (2000).

[101] P. D. Desai, Inter. J. Thermophys. **8**, 763 (1987).

[102] J. Janssen, S. Surendralal, Y. Lysogorskiy, M. Todorova, T. Hickel, R. Drautz, and J. Neugebauer, Comput. Mater. Sci. **163**, 24 (2019).

[103] L.-F. Zhu, J. Janssen, S. Ishibashi, F. Körmann, B. Grabowski, and J. Neugebauer, Comput. Mater. Sci. **187**, 110065 (2021).

[104] https://www.mpie.de/4008196/Software